CrystEngComm

Cytosine Monohydrate Under Mechanical Stress

Journal:	*CrystEngComm*
Manuscript ID	CE-ART-03-2023-000293.R1
Article Type:	Paper
Date Submitted by the Author:	25-Apr-2023
Complete List of Authors:	Fleming, Megan; Georgetown University, Department of Chemistry Hooks, Daniel; Los Alamos National Laboratory, Sigma Manufacturing Science, Center for Integrated Nanotechnologies McBride, Michael; Los Alamos National Laboratory, Sigma Manufacturing Science, Center for Integrated Nanotechnologies Li, Nan; Los Alamos National Laboratory, Center for Integrated Nanotechnologies Swift, Jennifer; Georgetown University, Department of Chemistry

Cytosine Monohydrate Under Mechanical Stress

Megan E. Fleming[a], Daniel E. Hooks[b,c], Michael McBride[b,c], Nan Li[c] and Jennifer A. Swift[a*]

[a]Georgetown University, Department of Chemistry, 37th and O Sts NW, Washington, DC 20057-1227, United States,
[b] Sigma Manufacturing Science, Los Alamos National Laboratory, Los Alamos, NM 87545, United States,
[c] Center for Integrated Nanotechnologies, Los Alamos National Laboratory, Los Alamos, NM 87545, United States

*jas2@georgetown.edu

ABSTRACT

Nanoindentation performed with a conospherical tip on the (100) face of cytosine monohydrate (CM) revealed a highly anisotropic response over a range of loads. Post-indent atomic force microscopy images identified an asymmetric deformation response owing to the pro-chiral structure of the surface. Activation of low rugosity slip planes induces movement of π-stacks rather than their displacement along the 1-dimensional hydrogen bonded ribbon direction. Anisotropy arises because slip can only propagate to one side of the indent, as the tip itself imparts a barrier to slip on the preferred plane thereby forcing the activation of secondary slip systems and pileup. The anisotropic deformation is of interest in relation to previous work which proposed a ribbon-rotation model to account for the topotactic conversion between CM and the product of its dehydration. The asymmetry in the nanomechanical properties exhibited by CM provides further support for the rotational model put forth and also serves to underscore the inherent relationship between a hydrate's mechanical properties and its solid state dehydration mechanism.

Introduction

A large percentage of molecular compounds, with applications ranging from explosives to pharmaceuticals, can crystallize as hydrates.[1-3] The relative stability of hydrated and anhydrous crystal forms depends on their structures and the environment (e.g. temperature, pressure, relative humidity). During manufacturing a wide range of environmental conditions may be encountered, and in some systems these environmental changes may induce phase transformations.[4-5] For hydrates in particular, high temperatures may result in water loss and the transition to a less hydrated or anhydrous form as well as particle fracture. Similarly, elevated pressures used in compaction steps in the preparation of pharmaceutical tablets or plastic bonded explosives can also lead to particle breakage or phase transformations. How and where a crystal will fracture are not always obvious, but are important aspects to consider since new surfaces are created.

The DNA nucleobase cytosine, a substructure of many modern pharmaceuticals (e.g. cidofovir, gemcitabine, lamivudine, citicoline),[6] crystallizes as a monohydrate (CM, refcode: CYTOSM)[7] from room temperature aqueous solutions. CM is stable under ambient conditions, though it dehydrates when subjected to elevated temperatures or low humidity environments.[8-13] In previous work,[14] we demonstrated through a combination of time-resolved synchrotron powder X-ray diffraction and TGA kinetic experiments that the hydrate to anhydrate solid state reaction is a reversible one-step process that does not appear to involve other crystalline intermediates. A molecular-level model based on water loss simultaneous with the cooperative rotation of 1-dimensional hydrogen bonded ribbons was proposed to account for the high degree of structure-transfer associated with the solid state reaction. In the proposed model, offset π-stacked antiparallel ribbons in CM cooperatively rotate to form orthogonal layers of face-face π-stacked parallel ribbons in the anhydrate.

Recognizing that cooperative molecular motion over multiple unit cells and large cell volume changes raises mechanical considerations, the nanomechanical properties of CM are the focus of the current study. The mechanical behavior of molecular crystals has been the subject of much interest[15-22] with nanoindentation methods[23-25] in particular emerging as an important tool for evaluating the plasticity or elasticity of single crystals, calculating fundamental parameters such as hardness and modulus, and establishing the relationship between structure and anisotropic behavior. When coupled with post-indent imaging, nanoindentation also enables the direct observation of slip systems[26] and fracture planes.[22, 27]

Experimental

Crystal Growth. Cytosine (≥ 99%) was purchased from Aldrich. Cytosine was dissolved in hot 18 MΩ ultrapure deionized water at a concentration of 4 mg/mL, pipette filtered into Pyrex petri dishes (100 x 10 mm) and cooled to room temperature. CM crystals typically appeared in 2-3 days as rectangular plates with large (100) faces (Fig. S1).

Crystals were viewed and photographed with an Olympus BX-50 polarizing microscope. Face indexing was determined by single crystal X-ray diffraction goniometry on a Bruker D8 diffractometer. The (100) plate face was additionally confirmed through oriented PXRD collected on a Rigaku MiniFlex II desktop X-ray diffractometer.

Nanoindentation. Samples were prepared by extracting individual CM crystals from the mother liquor and gently removing excess moisture with a Kimwipe. Single CM crystals with the (100) plate face exposed were affixed to a puck sample holder (Ted Pella Inc AFM Specimen Discs, 12

mm diameter) with a thin layer of cyanoacrylate glue. Multiple crystals grown under identical conditions were examined.

Nanoindentation experiments were performed on a Bruker Hysitron 950 Triboindenter with a low load QSM transducer. Indentations were made using a 90° conospherical tip, the radius (0.906 μm) of which was determined from elastic loading experiments on fused quartz using a classic Hertzian loading profile. Optimized indentation conditions were determined by testing several load control and displacement control functions. Unless otherwise indicated, all reported experimental data were collected with a 20 s load - 150 s hold - 20 s unload profile with a linear loading and unloading rate of 5 μN/s. Indentations were separated by at least 20 μm to prevent overlapping plastic zones.

Hardness *(H)* and reduced modulus (E_r) were calculated from experiments with a maximum load of 1000 μN. Hardness was calculated according to Eq. 1 where P_{max} is the maximum load and A is the tip-sample contact area.

$$H = P_{max}/A \quad (1)$$

The reduced modulus was calculated according to Eq. 2 from the elastic unloading curve where S is stiffness and β is a constant related to the shape of the indenter tip.

$$E_r = \frac{S\sqrt{\pi}}{2\beta\sqrt{A}} \quad (2)$$

The effect of load on the H and E_r was determined through a series of indents varying load in the range of 100 μN to 8000 μN.

Atomic Force Microscopy (AFM). Topographical images of (100) CM crystal surfaces pre- and post-indent were collected on a Bruker Dimension Icon AFM with a Bruker ScanAsyst-Air silicon tip on a nitride lever (cantilever: T = 650 nm, L = 115 μm, W = 25 μm, f_0 = 70 KHz, K = 0.4 N/m). Imaging was performed in the ScanAsyst PeakForce tapping mode. The same sample pucks with affixed CM crystals from nanoindentation experiments were mounted on the AFM stage. The root mean square roughness (Rq) on (100) CM was calculated using Eq. 3.

$$R_q = \sqrt{\frac{\sum(Z_i)^2}{N}} \qquad (3)$$

In this equation, Z is the vertical distance of a point to the mean plane surface, and N is the number of data points in the image area. Reported values are an average of measurements on 3 single crystals.

Results & Discussion

Cytosine monohydrate (CM) crystallizes from room temperature aqueous solutions as transparent rectangular plates that can grow to mm - cm sizes. The largest face is (100) with smaller side faces (010) and (001) and occasionally (101), (102) or (110). A packing diagram of CM with the major features of interest indicated appears in Fig. 1. All intermolecular distances refer to refcode CYTOSM11 ($P2_1/c$: a = 7.783 Å, b = 9.825 Å, c = 7.668 Å, β = 99.57°).[28] Water

molecules hydrogen bond to cytosine through O_w-H..O (1.95 Å and 2.04 Å) and NH_2…O_w (2.13 Å). Along the *b*-axis, cytosine molecules assemble into polar 1-dimensional hydrogen bonded ribbons formed via N…H-N and NH_2..O (2.09 and 2.15 Å, respectively). Ribbons with an antiparallel alignment π stack (3.83 Å repeat) along the *c*-axis to create dense layers in the *bc*-plane. All ribbons are tilted by 26.6° relative to the plate face. On the (100) surface, the tilt is toward the -*c* direction, and on the (-100) face the tilt is toward the +*c* direction.

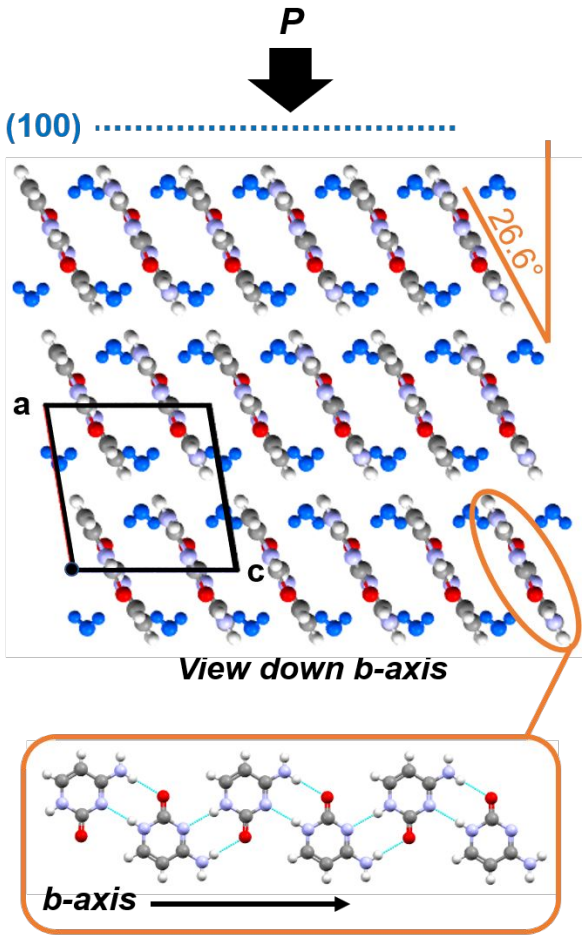

Fig. 1 Cytosine monohydrate (CM) structure viewed down the *b*-axis. Water molecules are colored blue. One-dimensional hydrogen bonded ribbons with an antiparallel orientation π-stack into dense (100) layers. Ribbons are tilted by 26.6° relative to the (100) surface.

CM Nanoindentation - Hardness and Modulus. All nanoindentation experiments were performed on the {100} CM faces of single crystals. The crystal orientation was established based on

morphology, as plates are elongated along the *b*-axis. Distinguishing (100) and (-100) is difficult using morphology alone but possible with single crystal X-ray diffraction. The (100) and (-100) faces are mirror images of one another, as are the indent patterns on them. Previous studies[29-30] have shown that for highly anisotropic samples, modulus and hardness measurements can vary depending on the relative orientation of a conventional Berkovich tip and crystal surface. To avoid the potential convolution of tip-sample contact anisotropies, all nanoindentation experiments were performed with a conospherical indenter tip, the radius (0.906 μm) of which was determined from elastic loading experiments.[31]

Loads ranging from 100-8000 μN were initially tested, with representative load-displacement curves shown in Fig. 2. The total displacement increased with load, but at all forces greater than 100 μN smaller discontinuities or "pop-ins" were observed in the load portion of the curve. Sudden yielding of the material under uniaxial loads is not uncommon for molecular crystals given their low symmetry. The magnitude of the displacement associated with each pop-in event varied from 5 – 40 nm (~6-52 cytosine layers), though larger excursions up to ~ 85nm were sometimes observed at the highest loads. There was no discernable trend in the number of pop-in events as a function of load or from crystal to crystal (Fig. S2). The irregular step excursions observed in the load-depth profiles indicate that the deformation is not homogeneously activated, but rather due to sub-surface defects.[32] Pop-outs were not observed in any unloading curves, making it unlikely that a reversible phase transformation occurs at the force loads used. Plots of the modulus and hardness derived from all load-displacement curves with depths between 100 – 1000 nm revealed an inherent scaling factor in the measurements (Fig. S4). Higher applied loads correlated not only with a greater contact depth but also an increase in stiffness.

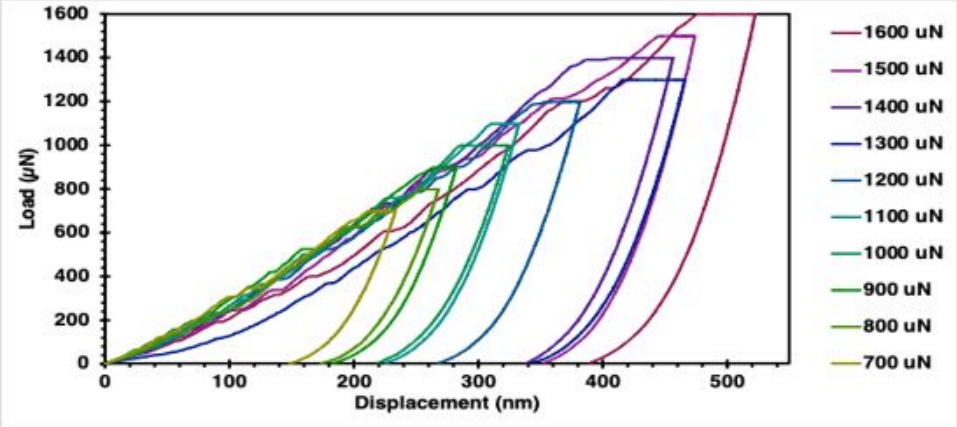

Fig. 2 Load-displacement profiles with varying maximum loads on CM (100).

To calculate accurate modulus and hardness values from load-displacement curves, the contact geometry model for conospherical tips is considered valid so long as the inherent surface roughness is < 5-10 % of the indent depth. Atomic force microscopy (AFM) measurements on visually smooth regions of (100) CM had an average roughness of 11.39 ± 4.00 nm. We therefore targeted a contact depth range of 250-350 nm which could be reliably achieved with an indenting force of 1000 μN and an optimized load profile of 20 s (load) - 150 s (hold) and 20 s (unload). A total of 64 indents (no. crystals = 6) in the desired range were collected. Average modulus and hardness values were E_r = 13.47 ± 0.84 GPa and H = 0.58 ± 0.03 GPa, respectively. These values fall within the expected range for molecular crystals.[19, 29, 33]

Post-indentation AFM Imaging. CM faces indented with loads from 1000 - 8000 μN were subsequently imaged with PeakForce tapping mode AFM (Fig. 3A). Close-ups of individual indents made with 1000 μN and 8000 μN force are shown in Fig. 3B-E. All indents show a similar anisotropic response. Pile up adjacent to each indent is observed only along the ± *c*-axis directions, with the pileup volume noticeably larger in the +*c* direction (right) compared to the -*c* direction (left) (Fig. 3F).

Cracks paralleling the ± *b*-axis emerge from the edges of the 8000 μN indent, though cracking is not observed in the shallower indents made at 1000 μN. Strictly speaking cracking violates conditions required to determine slip systems, but inferences can still be made. Projecting zone axes for fracture and deformation normal to the indentation plane, the cleavage is consistent with (001) or other (h 0 l) planes. Fracture along (102) or (104) seems most probable, since these are slip planes predicted by the CSD-Particle module in *Mercury* (Fig. S5).[34] The (102) cleavage plane is indicated by dashed lines in Fig. 3G.

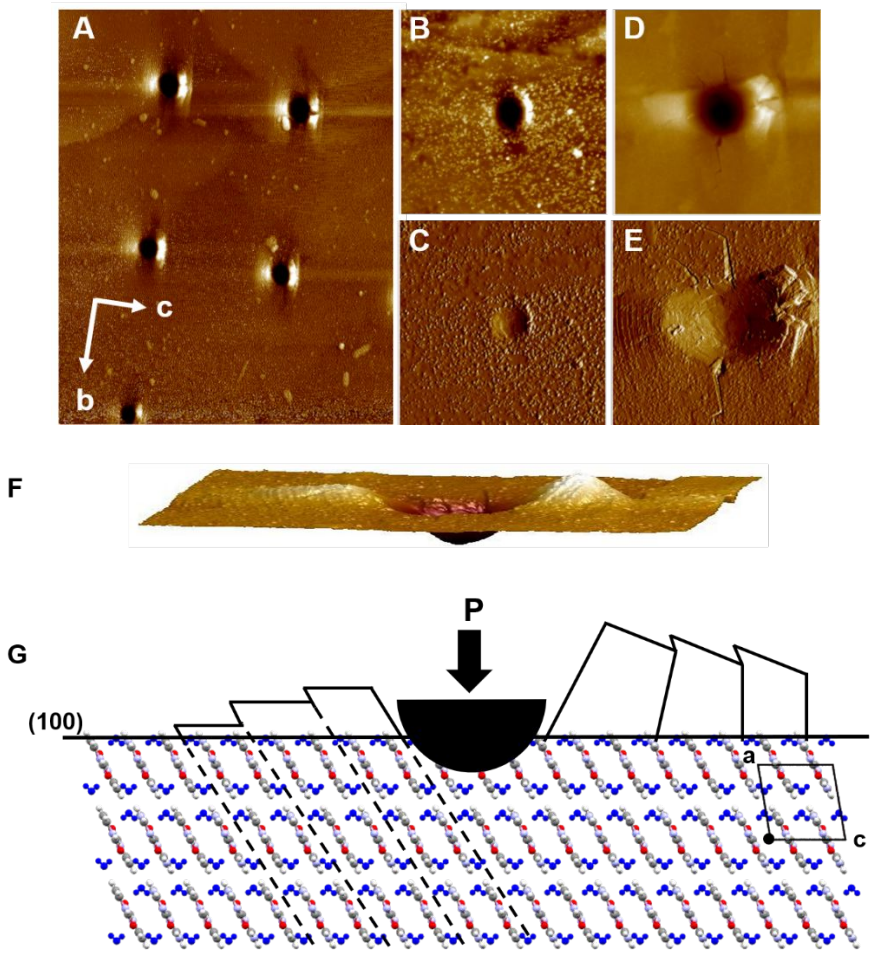

Fig. 3 (A) AFM image of the (100) CM surface after multiple indents with a conospherical tip with increasing forces from 1000 - 8000 μN. (B, C) Close up of a 1000 μN indent in height and deflection mode. Images are (9.4 μm)^2. (D, E) Close up of an 8000 μN indent in height and deflection mode. Images are (15 μm)^2 and (10 μm)^2, respectively. (F) Side-on view of the 8000

μN indent viewed edge-on. (G) Schematic of the indent and anisotropic pileup along the + and – *c*-axes. Dashed lines correspond to the (102) plane.

The crystal structure viewed normal to the (100) plane and the indent image in the same orientation are shown in Fig. 4 with the cleavage plane and slip trace directions overlaid. On the left side of the indent, the (102) slip propagates to the surface and associated slip steps are observed extending away from the indent. The curvature along these steps is indicative of cross-slip, perhaps onto other observed slip planes. Note that those same slip steps do not manifest to the right of the indent, and a different pile-up feature is observed. Along the +*c* direction, slip on (102) to the surface is immediately impeded by the indenter itself, requiring subsequent slip onto different planes. Angular facets on this larger pileup are consistent with dominant slip on (021)/(0-21), (012)/(0-12) and (014)/(0-14), indicated in yellow, blue and green, respectively. The (014) is not a calculated slip plane, however (114) and (214) planes are predicted and are indistinguishable from (014) in the AFM image. The jogs in the crack seem to also align with these slip step directions.

The consistency of the anisotropic deformation pattern and resolution of cleavage and slip traces was observed across multiple CM crystals. A similar response has been observed in other molecular systems where deformation mechanisms are limited due to crystal structure and/or lattice symmetry. For example in studies on the secondary explosive RDX,[35] the barrier to continued slip on the preferred plane imparted by the tip itself revealed secondary slip mechanisms as the pileup activates the less-preferred slip systems. Even in higher symmetry materials such as titanium, anisotropic behavior has been observed over a wide load range, with cleavage and increasing slip more evident at higher loads.[36]

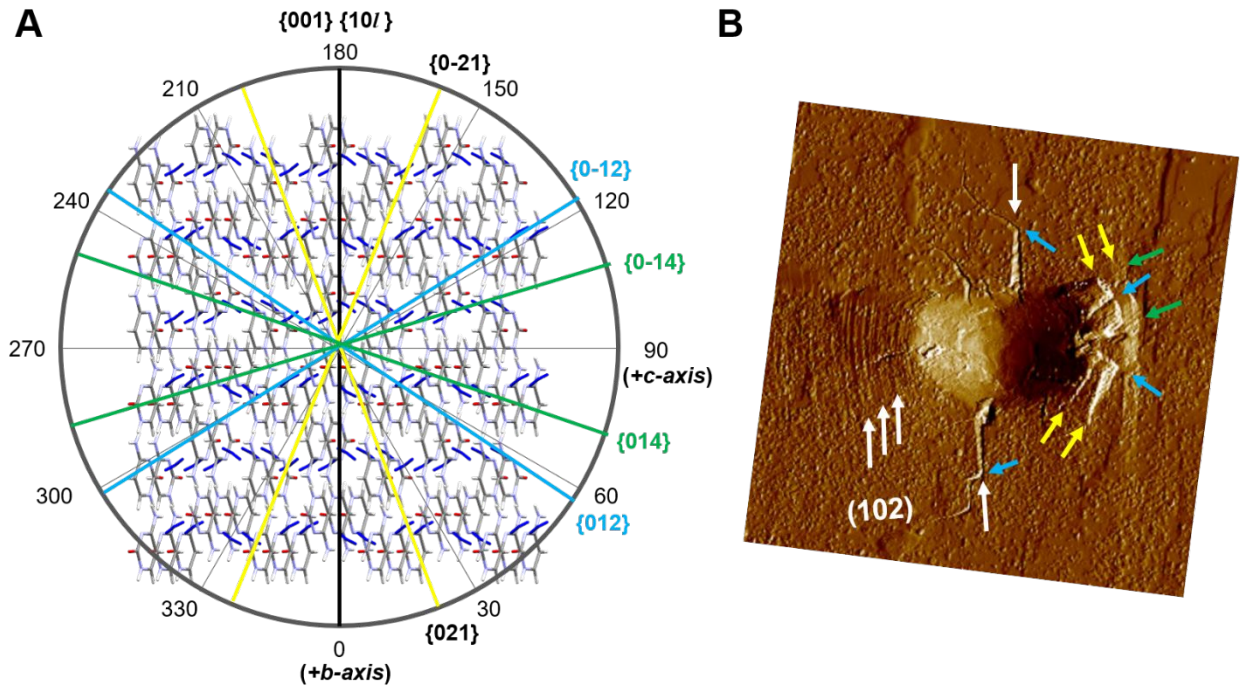

Fig. 4 (A) Schematic of the molecular packing viewed normal to the (100) CM face with projected zone axes overlaid. Water molecules are dark blue. (B) AFM image of an 8000 μN indent in the same orientation. The yellow, blue and green orientations on the left correspond to the same colored arrows on the right. The (10*l*) cleavage plane is indicated by the white arrows.

Implications of the Anisotropic Response. This anisotropy can be rationalized based on the interactions between molecules in the (100) plane. Recall that the 1-dimensional cytosine ribbons align along ± *b*-axis and π-stack along the ± *c*-axis. Although the hydrogen bonded ribbons are essentially flat, the absence of pile up along the ± *b*-axis indicates that ribbons cannot easily translate past one another to alleviate uniaxial stress. Translation would require a change in the π-stacking interactions between adjacent ribbons. Deformation preferentially occurs orthogonal to the ribbon direction, though ± *c* directions are not equivalent. As shown in Figs. 1 & 3G, the ribbons tilt toward the -*c* direction on (100), making it possible for slip to propagate smoothly in that direction even several μm away from the indent site. Since this is not possible in the +*c* direction, pileup activates secondary slip mechanisms.

Conclusions

The deformation patterns observed in CM are consistent with the activation of motion in the π-stacking direction that was previously proposed in the dehydration of CM to its anhydrate, Cd.[14] In that work, dehydration via concerted water loss and ribbon rotation were rationalized in terms of least-motion principles even though the reaction has a large associated 18.3% volume change. While there is no evidence to suggest that indentation at these forces results in water loss, the current nanoindentation studies provide additional support for the proposed ribbon-rotation model. It seems that the inherent mechanical properties of CM provide an additional bias favoring motion in some π stacking directions that goes beyond topochemical arguments. Notably CM belongs to space group $P2_1/c$, one of the most common for molecular crystals. We expect that other molecular crystals may exhibit an analogous anisotropic response in cases where the dominant slip plane is far from perpendicular to the direction of the applied uniaxial force.

Conflicts of Interest

The authors declare no conflicts of interest.

Acknowledgements

We are grateful for financial support provided by the National Science Foundation (DMR 2004435). Conversations with David Bahr were helpful in interpreting some of the indentation results. This work was performed, in part, at the Center for Integrated Nanotechnologies, an Office of Science User Facility operated for the U.S. Department of Energy (DOE) Office of Science. Los Alamos National Laboratory, an affirmative action equal opportunity employer, is managed

by Triad National Security, LLC for the U.S. Department of Energy's NNSA, under contract 89233218CNA000001.

References

1. Werner, J. E.; Swift, J. A., Data mining the Cambridge Structural Database for hydrate–anhydrate pairs with SMILES strings. *CrystEngComm* **2020,** (22), 7290-7297.
2. Healy, A. M.; Worku, Z. A.; Kumar, D.; Madi, A. M., Pharmaceutical solvates, hydrates and amorphous forms: A special emphasis on cocrystals. *Adv. Drug Deliver. Rev.* **2017,** *117*, 25-46.
3. Griesser, U. J., The importance of solvates. In *Polymorphism in the Pharmaceutical Industry*, Hilfiker, R., Ed. Wiley-VCH: Weinheim, 2006; pp 211-257.
4. Brandel, C.; Cartigny, Y.; Couvrat, N.; Eusébio, M. E. S.; Canotilho, J.; Petit, S.; Coquerel, G., Mechanisms of Reversible Phase Transitions in Molecular Crystals: Case of Ciclopirox. *Chem. Mater.* **2015,** *27* (18), 6360-6373.
5. Thakral, N. K.; Mohapatra, S.; Stephenson, G. A.; Suryanarayanan, R., Compression-Induced Crystallization of Amorphous Indomethacin in Tablets: Characterization of Spatial Heterogeneity by Two-Dimensional X-ray Diffractometry. *Mol. Pharm.* **2014,** *12* (1), 253-263.
6. Wishart, D. S.; Feunang, Y. D.; Guo, A. C.; Lo, E. J.; Marcu, A.; Grant, J. R.; Sajed, T.; Johnson, D.; Li, C.; Sayeeda, Z.; Assempour, N.; Iynkkaran, I.; Liu, Y.; Maciejewski, A.; Gale, N.; Wilson, A.; Chin, L.; Cummings, R.; Le, D.; Pon, A.; Knox, C.; Wilson, M., DrugBank 5.0: a major update to the DrugBank database for 2018. *Nucleic Acids Res.* **2018,** *46* (D1), D1074-D1082.
7. Jeffrey, G. A.; Kinoshita, Y., The crystal structure of cytosine monohydrate. *Acta Crystallographica* **1963,** *16* (1), 20-28.
8. Braun, D. E.; Griesser, U. J., Prediction and experimental validation of solid solutions and isopolymorphs of cytosine/5-flucytosine. *CrystEngComm* **2017,** *19* (26), 3566-3572.
9. Braun, D. E.; Kahlenberg, V.; Griesser, U. J., Experimental and Computational Hydrate Screening: Cytosine, 5-Flucytosine, and Their Solid Solution. *Cryst. Growth Des.* **2017,** *17* (8), 4347-4364.
10. Kawasaki, T.; Hakoda, Y.; Mineki, H.; Suzuki, K.; Soai, K., Generation of Absolute Controlled Crystal Chirality by the Removal of Crystal Water from Achiral Crystal of Nucleobase Cytosine. *J. Am. Chem. Soc.* **2010,** *132* (9), 2874-2875.
11. Mineki, H.; Kaimori, Y.; Kawasaki, T.; Matsumoto, A.; Soai, K., Enantiodivergent formation of a chiral cytosine crystal by removal of crystal water from an achiral monohydrate crystal under reduced pressure. *Tetrahedron: Asymmetry* **2013,** *24* (21), 1365-1367.
12. Perrier, P.; Byrn, S. R., Influence of crystal packing on the solid-state desolvation of purine and pyrimidine hydrates: loss of water of crystallization from thymine monohydrate, cytosine monohydrate, 5-nitrouracil monohydrate, and 2'-deoxyadenosine monohydrate. *J. Org. Chem.* **1982,** *47* (24), 4671-4676.
13. Martel, P.; Powell, B. M., Dehydration of cytosine monohydrate at physiological temperatures. *Biophys. J.* **1983,** *41* (1), 91-93.

14. Fleming, M. E.; Watts, T. A.; McKenna, K. A.; Miehls, E. K.; Swift, J. A., Cooperative Rotational Motion Triggered by a Water Switch: Dehydration and Rehydration of Cytosine Monohydrate. *Cryst. Growth Des.* **2022,** *22* (12), 7443-7451.
15. Gabriele, B. P. A.; Williams, C. J.; Lauer, M. E.; Derby, B.; Cruz-Cabeza, A. J., Probing anisotropic mechanical behaviour in carbamazepine form III. *CrystEngComm* **2021,** *23* (34), 5826-5838.
16. Liu, F.; Hooks, D. E.; Li, N.; Mara, N. A.; Swift, J. A., Mechanical Properties of Anhydrous and Hydrated Uric Acid Crystals. *Chem. Mater.* **2018,** *30* (11), 3798-3805.
17. Saha, S.; Mishra, M. K.; Reddy, C. M.; Desiraju, G. R., From Molecules to Interactions to Crystal Engineering: Mechanical Properties of Organic Solids. *Acc. Chem. Res.* **2018,** *51* (11), 2957-2967.
18. Das, S.; Mondal, A.; Reddy, C. M., Harnessing molecular rotations in plastic crystals: a holistic view for crystal engineering of adaptive soft materials. *Chem. Soc. Rev.* **2020,** *49* (24), 8878-8896.
19. Karothu, D. P.; Mahmoud Halabi, J.; Ahmed, E.; Ferreira, R.; Spackman, P. R.; Spackman, M. A.; Naumov, P., Global Analysis of the Mechanical Properties of Organic Crystals. *Angewandte Chemie International Edition English* **2022,** *61* (10), e202113988.
20. Wang, C.; Sun, C. C., Computational techniques for predicting mechanical properties of organic crystals - A systematic evaluation. *Mol. Pharm.* **2019,** *16* (4), 1732-1741.
21. Turner, M. J.; Thomas, S. P.; Shi, M. W.; Jayatilaka, D.; Spackman, M. A., Energy frameworks: insights into interaction anisotropy and the mechanical properties of molecular crystals. *Chem. Commun.* **2015,** *51* (18), 3735-3738.
22. Mannepalli, S.; Mangalampalli, K. S. R. N., Indentation Plasticity and Fracture Studies of Organic Crystals. *Crystals* **2017,** *7* (11), 324.
23. Ramamurty, U.; Jang, J., Nanoindentation for probing the mechanical behavior of molecular crystals–a review of the technique and how to use it. *CrystEngComm* **2014,** *16* (1), 12-23.
24. Gabriele, B. P. A.; Williams, C. J.; Lauer, M. E.; Derby, B.; Cruz-Cabeza, A. J., Nanoindentation of Molecular Crystals: Lessons Learned from Aspirin. *Cryst. Growth Des.* **2020,** *20* (9), 5956-5966.
25. Majumder, S.; Sun, C. C.; Mara, N. A., Nanomechanical testing in drug delivery: Theory, applications, and emerging trends. *Advanced Drug Delivery Reviews* **2022,** *183*, 114167.
26. Jing, Y.; Zhang, Y.; Blendell, J.; Koslowski, M.; Carvajal, M. T., Nanoindentation Method To Study Slip Planes in Molecular Crystals in a Systematic Manner. *Cryst. Growth Des.* **2011,** *11* (12), 5260-5267.
27. Burch, A. C.; Yeager, J. D.; Bahr, D. F., Indentation fracture behavior of energetic and inert molecular crystals. *J. Mater. Res.* **2019,** *34* (23), 3954-3963.
28. McClure, R. J.; Craven, B. M., New investigations of cytosine and its monohydrate. *Acta Cryst.* **1973,** *B29*, 1234-1238.
29. Taw, M.; Yeager, J.; Hooks, D.; Carvajal, T.; Bahr, D., The mechanical properties of as-grown noncubic organic molecular crystals assessed by nanoindentation *J. Mater. Res.* **2017,** *32* (14), 2728-2737.
30. Kim, Y.-Y.; Carloni, J. D.; Demarchi, B.; Sparks, D.; Reid, D. G.; Kunitake, M. E.; Tang, C. C.; Duer, M. J.; Freeman, C. L.; Pokroy, B.; Penkman, K.; Harding, J. H.; Estroff, L. A.; Baker, S. P.;

Meldrum, F. C., Tuning hardness in calcite by incorporation of amino acids. *Nat. Mater.* **2016,** *15*, 903-910.
31. Oliver, W. C.; Pharr, G. M., Measurement of hardness and elastic modulus by instrumented indentation: Advances in understanding and refinements to methodology. *J. Mater. Res.* **2004,** *19* (01), 3-20.
32. Ramos, K. J.; Bahr, D. F.; Hooks, D. E., Defect and surface asperity dependent yield during contact loading of an organic molecular single crystal. *Philos. Mag.* **2011,** *91* (7-9), 1276-1285.
33. Wang, C.; Sun, C. C., The landscape of mechanical properties of molecular crystals. *CrystEngComm* **2020,** *22* (7), 1149-1153.
34. Bryant, M. J.; Maloney, A. G. P.; Sykes, R. A., Predicting mechanical properties of crystalline materials through topological analysis. *CrystEngComm* **2018,** *20* (19), 2698-2704.
35. Ramos, K. J.; Hooks, D. E.; Bahr, D. F., Direct observation of plasticity and quantitative hardness measurements in single crystal cyclotrimethylene trinitramine by nanoindentation. *Philos. Mag.* **2009,** *89* (27), 2381-2402.
36. Nibur, K. A.; Bahr, D. F., Identifying slip systems around indentations in FCC metals. *Scripta Materialia* **2003,** *49* (11), 1055-1060.